Received: 29 May 2024 | Revised: 3 December 2024 | Accepted: 5 December 2024

DOI: 10.1002/qj.4923

Quarterly Journal of the Royal Meteorological Society RMetS

RESEARCH ARTICLE

Rain in convective downdraughts

G. G. Rooney[1] | **B. J. Shipway**[1] | **D. J. Parker**[2,3]

[1]Met Office, Exeter, UK

[2]National Centre for Atmospheric Science (NCAS), University of Leeds, Leeds, UK

[3]NORCE Norwegian Research Centre AS, Bergen, Norway

Correspondence
G. G. Rooney, Met Office, FitzRoy Road, Exeter, EX1 3AL, UK.
Email: gabriel.rooney@metoffice.gov.uk

Abstract

This study presents results from the simulation of idealised, rain-laden downdraughts using a large-eddy model. Each downdraught is initialised as a "cold, wet bubble", that is, a spherical/spheroidal region of the lower atmosphere with a negative potential-temperature perturbation and non-zero rain mixing ratio. The bubbles are statically unstable and evolve into downdraughts. Results are compared for two- and three-moment microphysics parametrisations. A tendency for larger raindrops to descend ahead of the cold air is observed, which is significant in some two-moment runs. The effects of this are interpreted in the context of fluid-dynamical studies of related phenomena. It is found that a drier environment has the effect of increasing cooling in the downdraught, but reduces the peak in downdraught speed. Both these effects stem from increased rain evaporation. A relatively heavy rain load leads to a narrower downdraught, through the suppression of internal (thermal-like) circulations. Downdraughts intensify, in both cooling and vertical velocity, in correlation with the initial bubble height-to-width ratio, being greatest for vertically stretched bubbles.

KEYWORDS

downdraught, large-eddy modelling, microphysics

1 | INTRODUCTION AND AIM

The aim of this study is to take the first steps towards characterising the structure and appearance of convective downdraughts, and observable *virga*, in relation to the underlying fluid dynamics.

Figure 1 is a photograph of a typical precipitation region beneath a convective cloud. It is characterised by some observable features: the virga are apparently laminar, near-vertical, and characterised by variations in density on a scale finer than the vertical scale. In terms of the fluid dynamics of this region, we can infer some conclusions immediately, in particular that this precipitation region has relatively little turbulence, in contrast to the convectively ascending part of the cumulonimbus cloud.

Arising from this observation, this work examines the relationship between the precipitation region and the descending downdraught. Specifically, we consider how the characteristics of the falling precipitation, as observed in virga, relate to the likely intensity of the downdraught.

We consider the related fluid-dynamical literature along with some conclusions drawn from very simple idealised numerical simulations. These are intended as a limited but systematic study of idealised downdraught initiation, to help isolate and describe the different influences.

FIGURE 1 Precipitating cumulus.

We conclude by considering some other aspects of the flow, in particular the vertical striations of the precipitation, which will need further study.

2 | BACKGROUND

2.1 | Convective downdraughts

Localised downdraughts from convective precipitation are the source of convective cold pools, that is, masses of relatively cold, near-surface air which spread out due to their negative buoyancy. Knupp and Cotton (1985) distinguished these from downdraughts within non-precipitating cumulus clouds, which they categorised as usually less intense.

Cold pools are hazards due to their extreme near-surface wind gusts and ability to transport dust (Linden & Simpson, 1985; Rooney, 2017). An interesting summary of early cold-pool and downdraught research by Fujita is given by Wilson and Wakimoto (2001, and see references therein). Cold pools also prolong the diurnal peak of convection and precipitation and produce large perturbations in surface fluxes (Grant & van den Heever, 2018; Joseph *et al.*, 2021; Sakaeda & Torri, 2023). Thus it is important to represent cold-pool effects in numerical weather models (Hirt *et al.*, 2020; Rio *et al.*, 2013; Rooney *et al.*, 2022), and hence downdraughts have long been phenomena of interest (Knupp & Cotton, 1985).

Dynamical modelling of downdraughts in numerical weather models is challenging, due to their relatively small horizontal scale of the order of a kilometre, extreme vertical velocities, and formation within convective clouds (Bolgiani *et al.*, 2020). Wakimoto (2001) and Giangrande *et al.* (2013) suggested that precipitation evaporation and mass-loading can each be dynamically significant from case to case, perhaps in equal significance (see also Knupp, 1988; Mallinson & Lasher-Trapp, 2019). The modelling of Torri and Kuang (2016, 2017) found a greater energetic input from evaporation, although this will depend on the state of the environment.

Observation of downdraught properties can also present a challenge; however, their effects may be inferred to some extent from the properties of the cold pools they engender. A recent observational study by Liu *et al.* (2022) found that convective rainfall was effective at cooling near-surface air and that surface relative humidity of approximately 70% was a threshold value, inasmuch as there was greater cooling for humidity lower than this. Chandra *et al.* (2018) observed that cold-pool "strength"—whereby they meant surface (1-m altitude) temperature reduction from the background—correlated with dryness of the mid-troposphere. Kirsch *et al.* (2021) defined cold-pool strength as the temperature perturbation at an observation height of 2 m, and found this correlated with dryness of the near-surface layer. Kruse *et al.* (2022) analysed 10-m temperatures in a long-term study and found a similar correlation, with rainfall intensity as an additional factor. (Note that the studies above span a variety of environmental conditions.)

Takemi (2006) defined squall-line strength in terms of precipitation intensity, and linked an increase in this measure with moister boundary layers and drier mid-layers. Takemi (2006) suggested that the mechanism for this correlation depended on the associated convective available potential energy and wind shear for convective organisation. James and Markowski (2010) defined cold-pool strength as the integrated negative buoyancy perturbation through the depth of the cold pool, but characterised the downdraught intensity in terms of its mass flux. They found that the enhanced evaporation with a drier mid-layer was, by itself, insufficient to strengthen downdraughts, and suggested that the available observational evidence was equivocal in this regard.

One-dimensional (vertical) models of multiphase downdraughts, such as might be used in subgrid parametrisation, were presented by Kamburova and Ludlam (1966) and Srivastava (1985). These focused on liquid (rain) as the particulate phase; however, ice was also considered later by Srivastava (1987). They concluded that downdraught penetration was weaker in a stable environment and more effective when the environment was closer to neutral (dry adiabatic lapse rate), as would be expected. [Srivastava (1985) suggested that vertical oscillations may occur if stability is sufficiently high, which would be the downward equivalent of cloud-top "overshooting" in an updraught.] They found downdraught intensity to be correlated with high drop concentration and small drop size.

Proctor (1989) used an axisymmetric numerical model to examine downdraught sensitivity to various factors, including environmental properties and downdraught size (width) and hydrometeor load. Results were assessed in terms of mainly cold-pool properties, but also downdraught velocity. One interesting finding was that wider downdraughts (which in that study contained proportionally more loading/forcing) had weaker vertical velocities, although the resulting cold-pool properties were generally magnified. The width dependence contrasts somewhat with an early modelling study by Takeda (1966). Aircraft observations of downdraught widths and speeds in a variety of environments have been tabulated by Knupp and Cotton (1985).

Similarly to the one-dimensional studies, considering downdraughts over the tropical ocean in a storm-resolving model, Windmiller *et al.* (2023) found that the rain amount/rate was determined largely by updraught properties and the environmental lapse rate. The downdraught speed was much less predictable by the same methodology, however.

Schiro and Neelin (2018) found the likely spatial origin of tropical continental downdraughts to lie within the lowest few kilometres of the atmosphere. The temporal origin is dictated by the preceding convective activity, although with a possible delay depending on atmospheric composition (Ross & Lasher-Trapp, 2024).

There have been numerous numerical weather-modelling studies investigating the dependence of the simulated downdraughts, cold pools, and further related weather features on microphysics schemes. Snook and Xue (2008, see also references therein to other studies) related variations in tornadogenesis to cold-pool strength (i.e., cooling), and hence to downdraught properties and ultimately microphysics. They found that smaller drop sizes lead to greater cooling in the downdraught. Morrison (2012) extended this line of study to aerosol interactions, highlighting that uncertainties in parametrisations can lead to first-order differences in results.

The microphysics of downdraughts is complicated when combined with multiphase dynamics. It is important to consider these flows dynamically as well as microphysically. The following subsection summarises some relevant factors when considering buoyancy effects in multiphase flows.

2.2 | Multiphase flows and buoyancy effects

Precipitation is composed of a spectrum of different-sized particles: solid ice and water drops. Fall speeds vary with particle size and composition. Evaporation/sublimation varies with the fall speed and the ambient conditions (Rogers & Yau, 1989, Ch.7). Any precipitation event is likely to be polydisperse, that is, composed of a variety of particle sizes. This means that there is a range of behaviour—from small particles, which can remain in suspension relative to the descent speed of a downdraught, to large particles falling rapidly and evaporating/subliming relatively little.

For fluid-only flows, a continuous stream of turbulent buoyant fluid moving vertically under gravity is usually termed a plume, and an isolated region of turbulent buoyant fluid moving likewise is termed a thermal; see Figure 2a,b. (Buoyancy here is taken to include either positive or negative buoyancy. Despite its suggestion of heat, the "thermal" name is applied to masses of cold air moving downward, as well as warm air moving upward.)

Precipitation in the atmosphere is one example of a multiphase buoyant flow containing particles or bubbles. Others include volcanic plumes (e.g. Woods & Bursik, 1991) or underwater dispersion of air bubbles or oil droplets (Boufadel *et al.*, 2020). These have often been studied or described as multiphase extensions of the single-phase case consisting of buoyant fluid only.

Particle terminal velocity depends on particle size. Depending on the speed of the fluid flow containing them, it is more likely that small particles will be passively advected and larger ones tend to fall out. For instance, Bush *et al.* (2003) show that, for a group of dense particles, fallout occurs when the speed of the turbulent "thermal" they produce reduces to below the particle terminal velocity; see Figure 2c–e. Yang *et al.* (2016, figure 8) show that the overshoot height of an aqueous bubble-plume in a stratified background is similar to that of single-phase plumes when the bubble size is small, but lower when it is larger. This is consistent with larger particles (bubbles) having a larger terminal velocity, hence being able to leave the plume body behind sooner, reducing plume-fluid penetration length.

Yang *et al.* (2016) classify particle (bubble) size using a non-dimensional ratio of terminal velocity to buoyant-flow velocity scale developed by Socolofsky and Adams (2005). This is very similar to the approach of Bush *et al.* (2003), and in line with the concept of the Stokes number, which compares particle inertia with flow inertia (Devenish *et al.*, 2012; Vaillancourt & Yau, 2000). The conclusion that may be drawn is that flow parameters, as well as particle size, are important when determining fallout. The corollary is that the degree of passive advection may vary in time for a particular flow situation, and is not necessarily possible to describe a priori using particle size alone.

There is evidence from Lai *et al.* (2016, e.g. figure 8) that polydisperse particle clusters experience vertical sorting under gravity. Hence larger particles fall faster/further. Particles that fall outside a turbulent fluid mass tend to

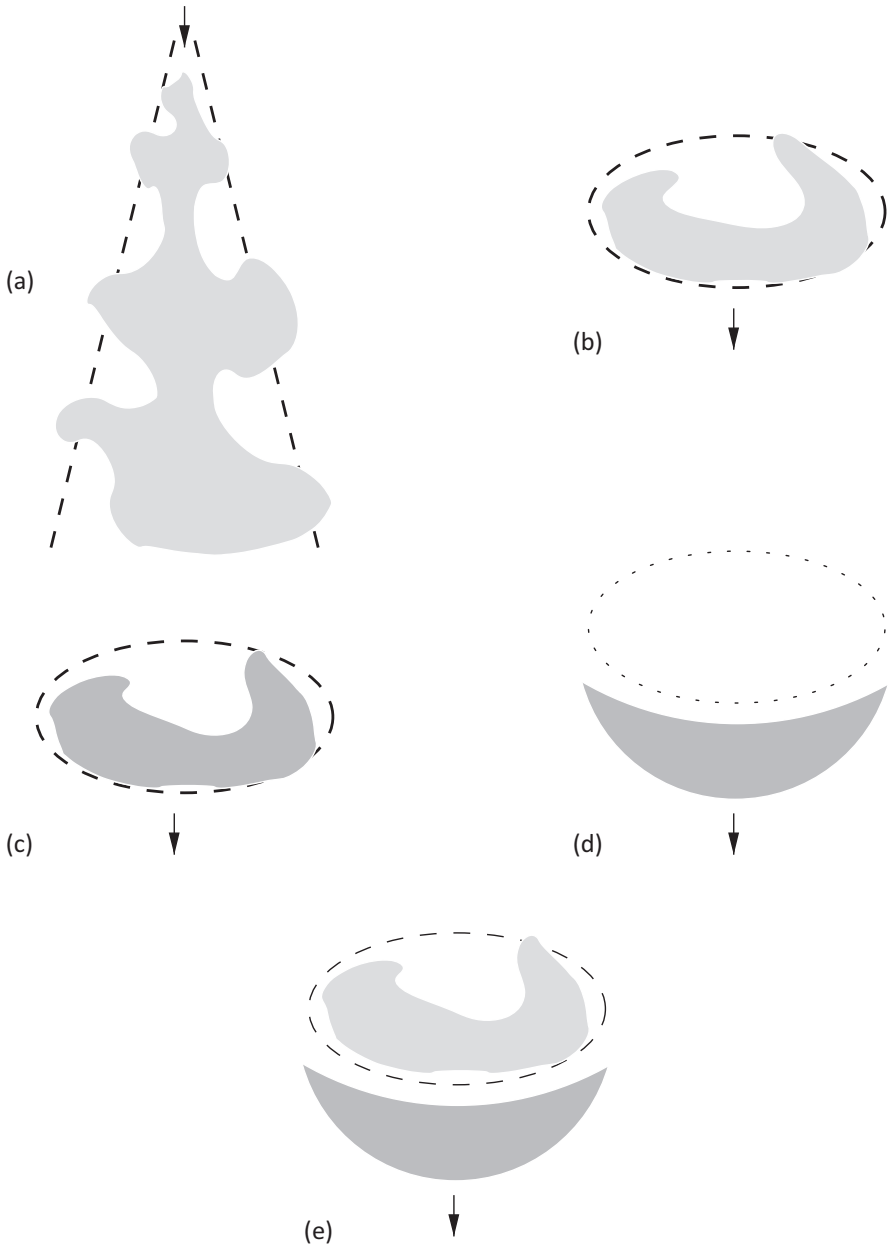

FIGURE 2 Sketch cross-sections of some gravity-driven flows, containing (a,b) fluid only, (c,d) particles only, or (e) both. (a) A plume from a small, steady source of negative buoyancy. The dashed line indicates the mean boundary, often thought of as conical. The shaded region is a sketch of the instantaneous flow, which can contain significant fluctuations. (b) A descending thermal composed of a localised region of dense fluid. As before, the dashed line indicates a notional mean boundary, which grows with time/distance due to entrainment. (c) A descending thermal composed of a suspension of particles. While the particles are in suspension, this is very similar to (b). (d) A fallout particle swarm, which may have previously been in thermal-like suspension in the region enclosed by the dotted line. (e) Fallout of particles from a negatively buoyant thermal. The buoyancy of the fluid may have been generated, for example, by evaporation while the particles were within the thermal, as in (c).

fall in straighter paths. A dense cluster of such particles is sometimes referred to as a "swarm" (Bush *et al.*, 2003; Slack, 1963). For a more continuous particle stream, there may be horizontal/radial sorting, with particles concentrated in less obviously turbulent flow near the centre of the descending region, but surrounded by turbulent fluid. Such structure was inferred from experimental observations by McDougall (1978), who developed a concentric integral model for bubble plumes. This was later adapted to model overshooting turbulent fountains and hence atmospheric phenomena (Bloomfield & Kerr, 2000; Devenish & Cerminara, 2018; McDougall, 1981). There is also evidence of this type of structure in the data of Bordoloi *et al.* (2020, fig. 9), and possibly also in the idealised simulations of Dawson *et al.* (2014).

Multiphase flows can be complicated further by the break-up or aggregation of elements in the particulate phase, for instance aggregation of raindrops or volcanic ash (Brown *et al.*, 2012).

3 | IDEALISED SIMULATIONS

3.1 | MONC and CASIM

Numerical experiments were performed using version vn1.0.0 of the Met Office–Natural Environment Research Council Cloud model (MONC: (Brown *et al.*, 2020)). MONC is a large-eddy model (LEM) designed for simulation of atmospheric processes. The experiments examined

an idealised "cold, rain-laden bubble", with the aim of identifying possible effects due to drop size on cold convective downdraughts. The "bubble" is a spherical/spheroidal region of the model domain, which is initialised differently from the background.

Microphysics in MONC was parametrised using version vn1.3 of CASIM (Cloud AeroSol Interacting Microphysics; Shipway & Hill, 2012; Field *et al.*, 2023). This version has three-moment microphysics disabled, so a modification was applied to re-enable this option as an alternative to the default two-moment configuration. Experiments were performed in both two- and three-moment modes.

Rain aggregation and sedimentation were always enabled (Field *et al.*, 2023). Rain evaporation and condensation were disabled for some experiments and enabled for others. The MONC solver was using the anelastic equations, and subgrid diffusion and turbulence were represented using a Smagorinsky subgrid scheme.

The numerical domain was 12.8 km in each horizontal direction and 5 km vertically. The grid resolution was 50 m in all directions. Top and bottom boundaries are free-slip and no-slip respectively, and lateral boundaries are periodic. The bottom boundary has a roughness-length representation of surface friction, with a roughness length of 0.2 mm.

MONC was run (as recommended) with a variable time step, chosen internally to ensure that advective and viscous processes satisfy a Courant–Friedrichs–Lewy (CFL) condition. The time-step upper and lower bounds were set to 1 and 0.01 s, respectively.

The bubble centre was at a height of 3 km, and horizontally at the domain centre. The majority of bubbles were spherical, with a radius of 500 m. Oblate and prolate spheroids with a vertical symmetry axis were also tested.

Outside the bubble, the domain was initialised with a potential temperature θ_0 of 300 K, uniform environmental relative humidity (RH_e) as given below, and no liquid (or solid) water content. Within the bubble, the properties to be initialised are the bubble relative humidity (RH_b), θ perturbation relative to the environment ($\Delta\theta$), and the rain content, in terms of rain mass mixing ratio q_r and number density of drops N_r.

To show the combined effects of the fields, an approximate buoyancy is calculated as

$$B = g\left(\frac{\Delta\theta}{\theta_0} + \epsilon(q_v - q_{v0}) - q_r\right), \quad (1)$$

in which g is the gravitational acceleration, $\epsilon = R_v/R_d - 1 \approx 0.61$ where R_v and R_d are the gas constants for water vapour and dry air respectively, q_v is the water vapour mixing ratio, and q_{v0} is the environment value at the same height (taken from a profile in one corner of the domain). This is based on the definition of virtual potential temperature (e.g. Tsonis, 2007), extended to account for water loading in the liquid phase (also known as density potential temperature e.g. Emanuel, 1994; Andrejczuk *et al.*, 2004).

3.2 | Bubble configurations

To explore the parameter space and demonstrate the different effects, several bubble configurations were used. Table 1 summarises these in terms of bubble properties and model switches. Several configurations were repeated at different values of RH_e, as specified hereafter in the text and figures.

The drop sizes may be characterised by the mean and mode diameters, $\overline{D}$ and D_Z respectively, as described in Appendix A. (In Table 1 q_r is given in g·kg $^{-1}$ rather than kg·kg $^{-1}$ as used in calculations.)

The configurations span two different values each of $\Delta\theta$, q_r, and raindrop size ($\propto (q_r/N_r)^{1/3}$). Rain evaporation

TABLE 1 Initial parameters and settings of the MONC experiments on idealised downdraughts. All bubbles are spherical with radius 500 m, except for O and P. Multiple values of RH_e are used, as specified in the text and figures.

Bubble type	$\Delta\theta$ (K)	q_r (g· kg^{-1})	N_r (m^{-3})	λ (m^{-1})	$\overline{D}$ (mm)	D_Z (mm)	RH_b %	Evap. and cond.
X	−2.0	5	3×10^5	1.4×10^4	0.25	0.18	95	off
Y	−0.5	5	3×10^5	1.4×10^4	0.25	0.18	95	off
Z	−2.0	1	6×10^4	1.4×10^4	0.25	0.18	95	off
A	−2.0	1	6×10^4	1.4×10^4	0.25	0.18	95	on
B	−2.0	1	1×10^3	3.6×10^3	1.0	0.7	95	on
C	−2.0	1	6×10^4	1.4×10^4	0.25	0.18	80	on
O	As A, but an oblate spheroid of the same volume.							
P	As A, but a prolate spheroid of the same volume.							

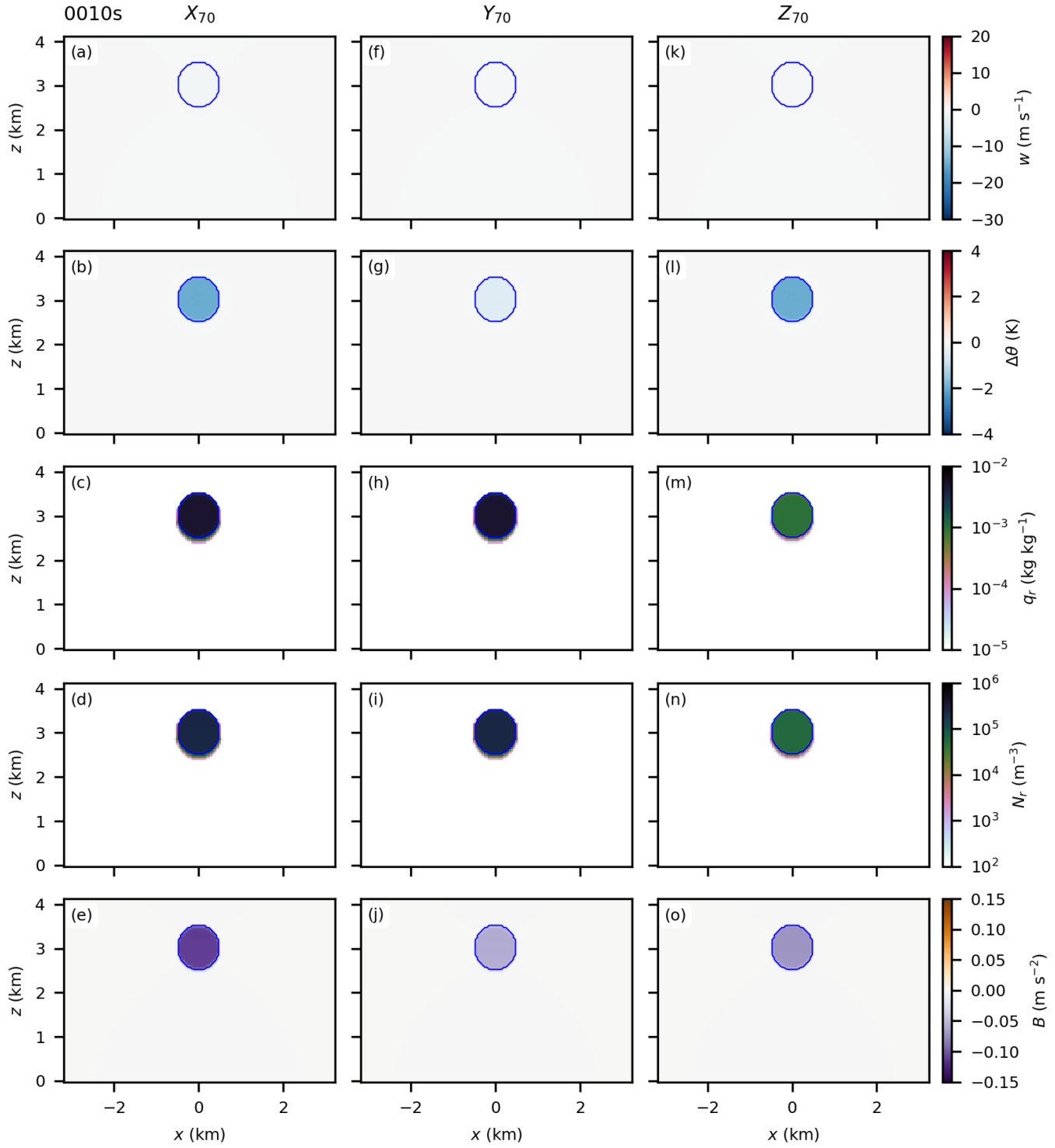

FIGURE 3 Simulation fields at 10 s, for experiments X–Z at $RH_e = 70\%$, indicated by the column headers. These experiments have evaporation and condensation disabled and different initial combinations of $\Delta\theta$ and q_r. From the top, the rows show vertical velocity, potential temperature perturbation, rain mass, rain number density, and buoyancy. Contours are drawn on all panels at a value of half the minimum $\Delta\theta$ in the domain at that time, for each experiment.

and condensation may be turned off or on. Different values of initial environmental relative humidity (RH_e) are tested, and bubble shape is also varied.

For configurations X, Y and Z, evaporation and condensation are disabled and the drop sizes are small. RH_e is set to 70%. $\Delta\theta$ and q_r are given either of two initial values.

Configuration A is the same as Z, except that evaporation and condensation are turned on. B is as A, except that initial N_r is reduced, leading to larger drop sizes. C is as A,

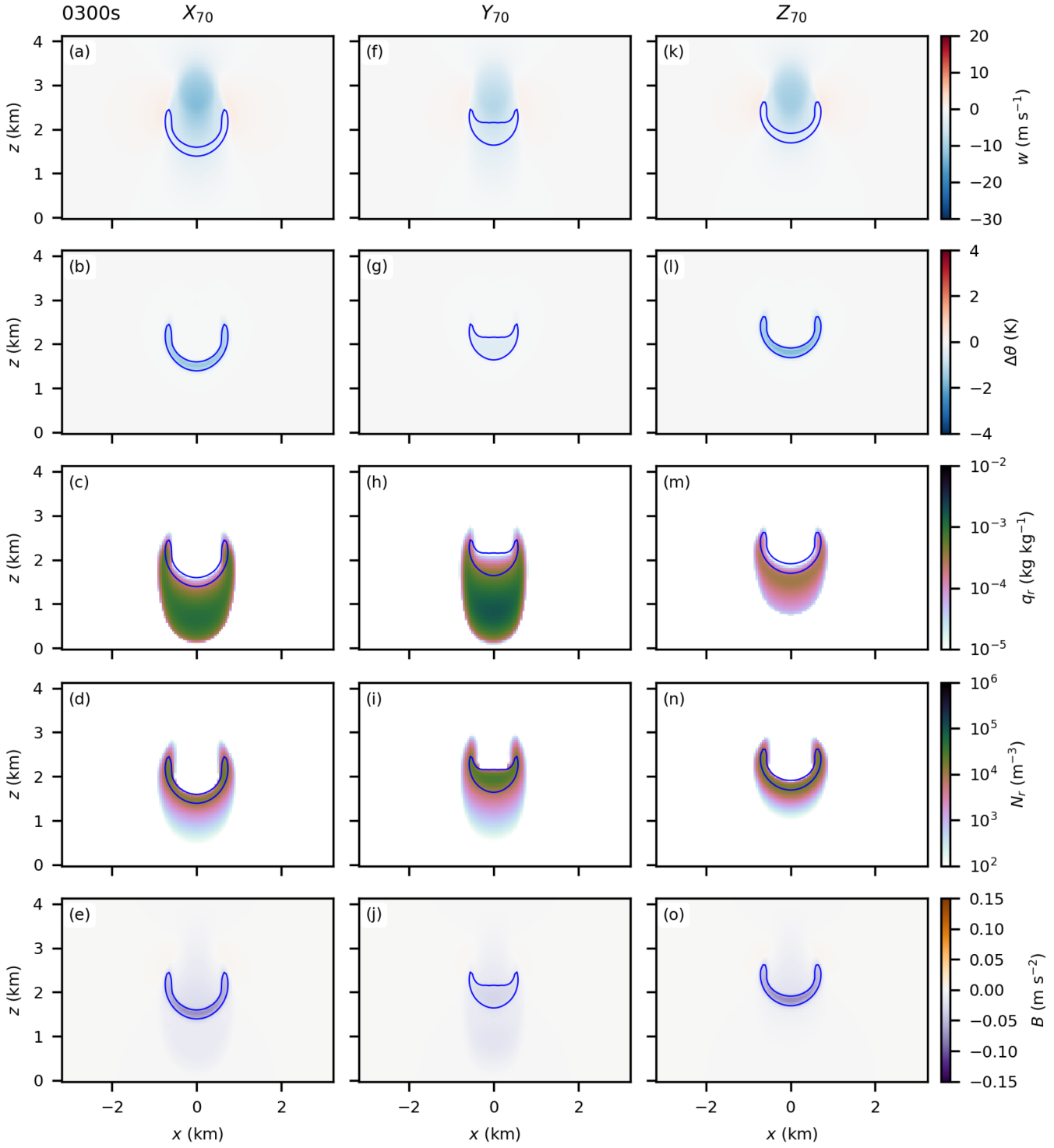

FIGURE 4 Simulation fields at 300 s for experiments X–Z at $RH_e = 70\%$. Panels as in Figure 3.

except that RH_b is reduced. These configurations are run at various values of RH_e.

O and P are as A, but instead of being spherical, the initial vertical axis of the bubble is respectively decreased or increased by a factor of two. In these configurations the initial bubble volume is kept unchanged by respectively increasing or decreasing each of the horizontal axes by a factor of $\sqrt{2}$; see Appendix B. Again, these configurations are run at various values of RH_e.

Most of the bubble configurations have an initial (negative) buoyancy within ±20% of A. The exception is X, which has an initial buoyancy approximately 50% larger

than A in magnitude, as it has the larger perturbation in both temperature and rain mass.

The model had zero initial velocity components. The initial configuration is unstable and the bubble initiates/becomes a downdraught. The simulations were allowed to run for 1000 s model time, at which point the downdraught has reached the domain floor and begun to spread out. Significant spreading would be affected by the domain boundaries, hence the simulations are terminated when the spread is still of small extent.

The majority of results presented here were generated using two-moment CASIM, which may be assumed hereafter unless stated otherwise. This bulk microphysics capability is widely used, as discussed for example by Field *et al.* (2023). However, as two-moment schemes may display excessive size sorting of hydrometeors (Milbrandt & McTaggart-Cowan, 2010), comparison with three-moment CASIM will also be presented, to demonstrate the differences arising from the use of a more sophisticated scheme.

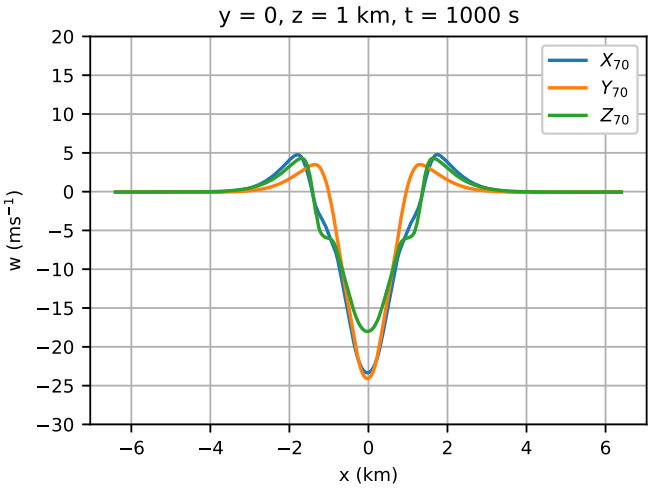

FIGURE 5 Vertical velocity profiles for configurations X–Z (without evaporation or condensation). These profiles are at a height of 1 km, horizontally through the centre of the domain, at the end of the experiment ($t = 1000$ s). For these experiments $RH_e = 70\%$, as indicated by the subscripts in the legend.

4 | EXPERIMENTS

4.1 | Temperature perturbation and rain mass

Experiments X, Y, Z compare the results of varying the initial temperature perturbation and rain mass. In these experiments, evaporation and condensation are disabled and RH_e is set at 70%. Figure 3 shows data from these experiments at 10 s after the start of each. The columns of Figure 3 correspond to the different experiments and the rows show cross-sections of different model fields: vertical velocity w, $\Delta\theta$, q_r, and N_r. In this figure and in the later cross-section figures, all panels also have a $\Delta\theta$ contour added, at a value equal to half the minimum $\Delta\theta$ in the domain at that time, for each experiment. This facilitates spatial comparison of the different fields within one experiment.

As prescribed in the initial conditions, the θ perturbation is smaller in Y than in X and Z, and q_r is smaller in Z than in X and Y (N_r is also proportionally lower in Z, to obtain equal initial drop-size distributions). At this point the bubbles are at the very early stage of transitioning into downdraughts and the vertical velocities are still relatively weak.

Figure 4 shows a later comparison, 300 s into the experiments. It may be seen that, in X and Y, the greater q_r has led to some drop aggregation and sedimentation, evident as precipitation fallout ahead of the descending front of the $\Delta\theta$ field. Since these experiments have rain evaporation turned off, there is no significant $\Delta\theta$ in this "fallout" region, but there is some indication of an associated perturbation in w there, compared with Z which does not exhibit significant fallout.

Figure 5 shows horizontal profiles of w through the centre of the domain at a height of 1 km, at the end of the experiments (1000 s), with subscripts in the legend indicating the value of RH_e. At this point, the central negative (vertically downward) "trough" in w is at its largest amplitude in each experiment. That is approximately in the range of $21 \pm 3\,\mathrm{m\cdot s^{-1}}$, which is of a similar order to previous assessments for these types of flows (e.g. Bolgiani *et al.*, 2020).

One interesting feature of this plot is that experiments X and Y with a larger initial q_r have a bigger trough, whereas X and Z with a larger (negative) initial $\Delta\theta$ have a wider region of upward flow on either side of the central trough. This shows that the increased rain mass increases the central acceleration of the downdraught, whereas the greater negative temperature perturbation reinforces the thermal-type vortex circulation around the edge.

Diagnostics that may be extracted from the data include the most negative θ perturbation within the domain at any time, $\Delta\theta_{min}$; its vertical position, z_θ; and a measure of the downdraught radius. The radius b is defined here as the maximum radius of any point with $\Delta\theta$ less than a fixed fraction of $\Delta\theta_{min}$ (which is negative). This fraction has been taken as 20%, which is the same as the threshold used similarly by Rooney (2015).

These diagnostics are plotted against time in Figure 6. The breaks in the trajectories of z_θ correspond to the gradient changes in the time evolution of $\Delta\theta_{min}$. The

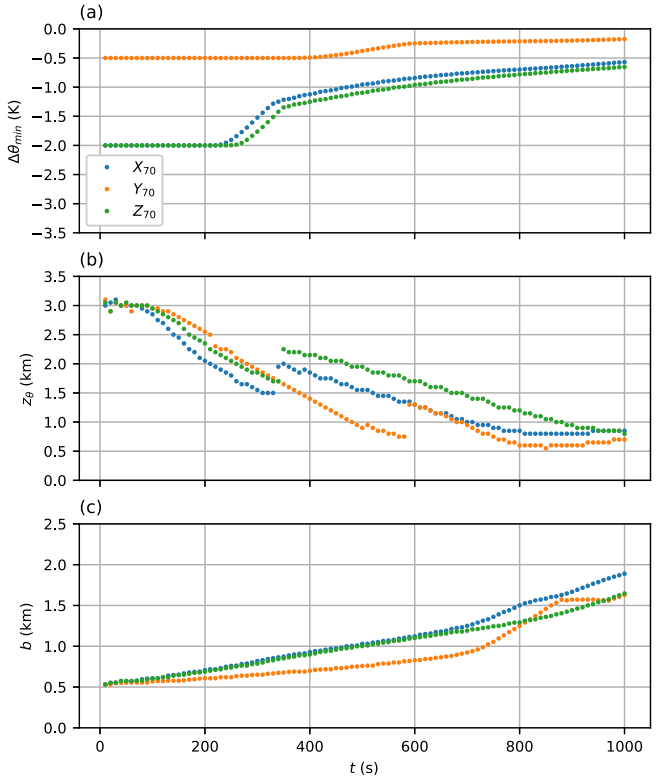

FIGURE 6 Time evolution of some quantities derived from experiments X–Z at $RH_e = 70\%$. (a) Most negative θ perturbation in the domain, $\Delta\theta_{min}$. (b) Vertical position of the most negative θ perturbation, z_θ. (c) Downdraught radius b, defined as the maximum radius of any point with $\Delta\theta < 0.2\Delta\theta_{min}$.

sudden shifts in position indicate that $\Delta\theta_{min}$ is initially in the central downdraught, but, as this rapidly diffuses away, the location of $\Delta\theta_{min}$ will then be found in the annular region, which is at a higher altitude. This happens later in Y, during its impingement phase, as its annular region is less pronounced in the downdraught.

The radial measure b of experiment Y indicates a narrower flow than that of X or Z. This agrees with the trend in Figure 5. It appears that the rain fallout dominates in Y, possibly inhibiting formation of a thermal vortex.

4.2 | Evaporation and drop size

Further microphysical effects on downdraught behaviour are explored here, by comparing configuration Z with A and B, in experiments in which RH_e is again initialised at 70%. A is the same as Z, but with rain evaporation and condensation enabled. B also has these processes enabled, and in addition a lower value of N_r, which leads to an increase in drop sizes.

Figures 7 and 8 show cross-sections of these experiments at times of 300 and 1000 s, respectively. (The first column of Figure 7 is the same as the last column of Figure 4.)

The larger drop sizes in B produce a faster fallout, which at 300 s has removed most of the rain mass from the thermal part of the downdraught. Also in B, drop aggregation has further reduced N_r to values no longer within the plotting range.

At 1000 s, fallout and evaporation have removed the rain mass in A and B, although not entirely in Z (which does not evaporate). The cross-sections show evidence of a spreading vortex-ring structure, similar to the front of an axisymmetric gravity current. This has a height of order 1 km, and hence is of a similar size to the initial bubble diameter. It appears slightly wider in A than in Z or B. The sustained downdraught has produced relatively dry air in the centre of the region, and a compensating weakly moist region uplifted around this, which shows up in the buoyancy field. Condensation in the uplifted regions of A and B produces some liquid water content there, as well as a positive potential temperature anomaly.

The vertical velocities show that the maximum vertical speeds close to the ground are much lower than those at altitude, as would be expected.

Figure 9 shows the corresponding vertical velocity profiles at the end of the experiments (1000 s). Unlike the experiments compared in Figure 5, these all have the same initial minimum buoyancy and seem more similar in shape, although A is slightly wider, as above.

Figure 10 shows the same derived quantities as in Figure 6. Experiment A with evaporation and smaller drops displays a significant boost to $\Delta\theta_{min}$ in the downdraught-descent phase. The others do not, due to disabled evaporation or rapid fallout of larger drops in Z and B respectively. It may be that this boost to the $\Delta\theta$ perturbation is the cause of the slightly wider profile of A.

4.3 | Humidity

Further experiments were carried out to explore the effect of variations in RH_e and/or RH_b. These were mainly experiments with configuration A and a varying RH_e, although configuration C was also tested, which is like A except with a lower RH_b value (80% instead of 95%). As above, particular experiments are denoted using the configuration letter with a subscript indicating the value of RH_e: for example, A_{50} denotes configuration A at $RH_e = 50\%$.

A change in RH_e would be expected to produce various effects with different implications for the buoyancy. For instance, for a drier environment, entrainment into the bubble would be expected to enhance raindrop evaporation, increasing the negative buoyancy contribution

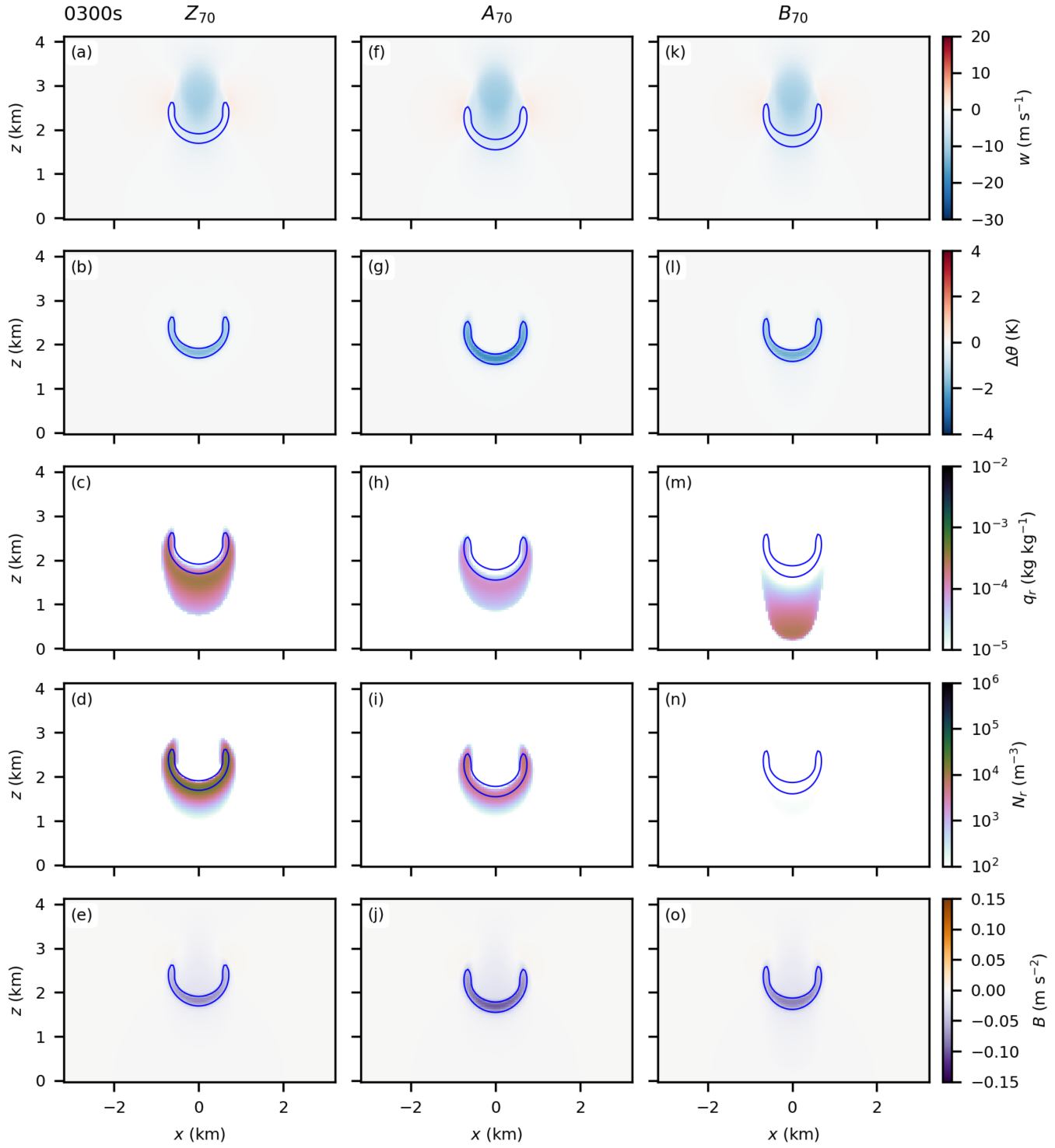

FIGURE 7 Simulation fields at 300 s, for experiments Z, A, and B at $RH_e = 70\%$. A and B have evaporation and condensation enabled. B has an initial drop-size distribution with a mean value greater than Z and A.

due to cooling. However the initial bubble would be relatively moister in the vapour phase, with a consequently greater initial positive buoyancy contribution. Increased evaporation will also accelerate the mass loss from the liquid phase, consequently reducing the gravity-driven particle–atmosphere momentum exchange which contributes to downdraught velocity. In a moister environment, vertical displacement of the environment may produce an updraught driven by latent heating. Hence the overall effect of these changes is difficult to predict.

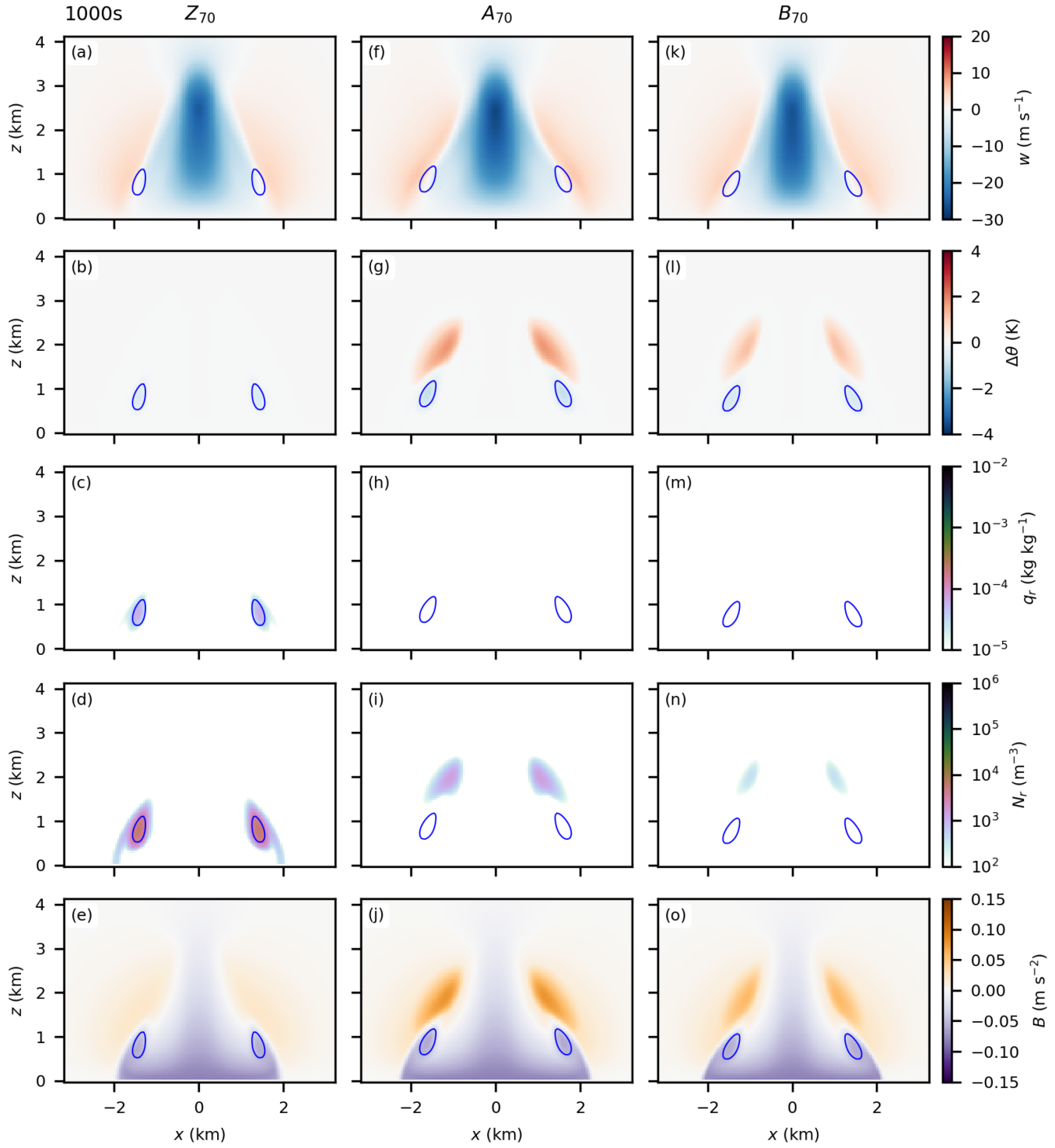

FIGURE 8 Simulation fields at 1000 s for experiments Z, A, and B at $RH_e = 70\%$. Panels as in Figure 7.

Cross-sections of the domain are not shown for these experiments. The end-of-experiment velocity profiles for A_{50}, A_{70}, and A_{90} are shown in Figure 11. These show significant differences, with the lowest-humidity environment producing the smallest downdraught velocity. The figure also shows the significant annular updraught in A_{90}. This had little positive buoyancy contribution from the water-vapour content of the initial bubble and also a more persistent rain mass, hence greater fallout, on account of reduced evaporation. These all tend to increase the downdraught velocity, but acceleration of the updraught has the effect of retarding the downdraught. In a test with

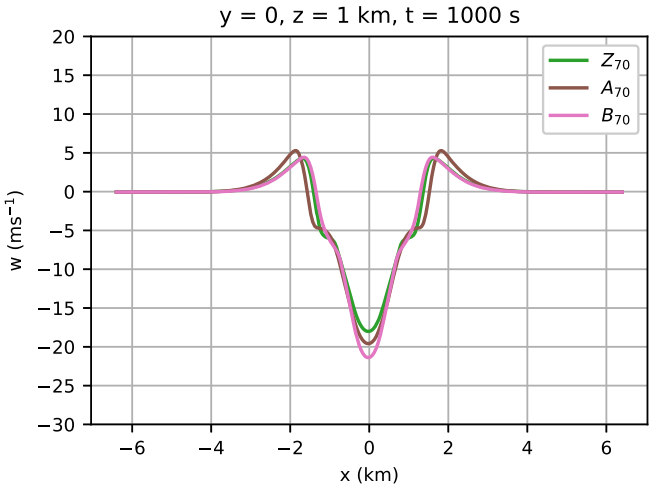

FIGURE 9 Vertical velocity profiles for experiments Z, A, and B at $RH_e = 70\%$. These profiles are at a height of 1 km, horizontally through the centre of the domain, at the end of the experiment ($t = 1000$ s).

condensation disabled (not shown), the downdraught velocity difference between A_{70} and A_{90} was then comparable with that between A_{50} and A_{70}.

Given that there is a significant initial difference between RH_b and RH_e for experiments A_{70} and A_{50}, further experiments were carried out with reduced differences, for example A_{85} or C_{70}, to see if the same trends are observed. These will be presented later, as additional points on the summary plots in Section 5.

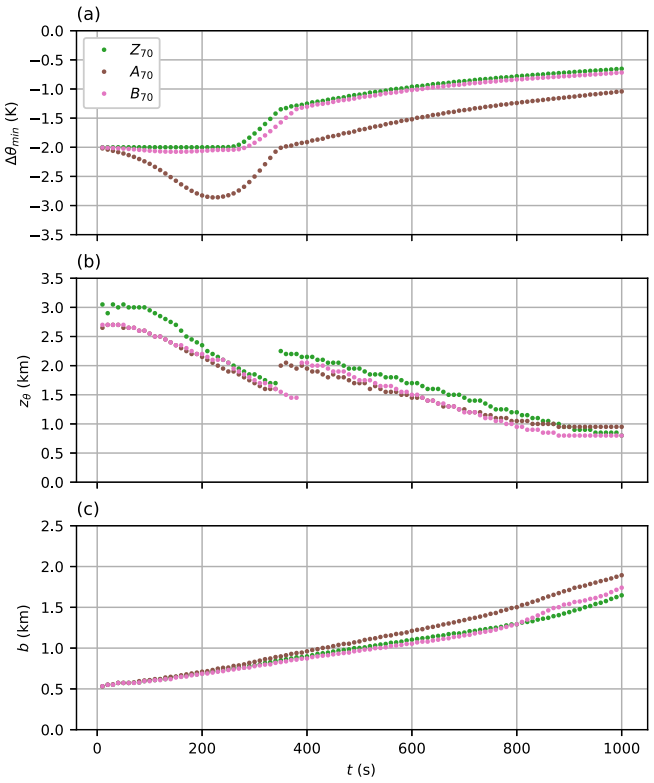

FIGURE 10 Time evolution of some quantities derived from experiments Z, A, and B at $RH_e = 70\%$. (a) Most negative θ perturbation in the domain, $\Delta\theta_{min}$. (b) Vertical position of the most negative θ perturbation, z_θ. (c) Downdraught radius b, defined as the maximum radius of any point with $\Delta\theta < 0.2\Delta\theta_{min}$.

4.4 | Initial bubble shape

Spheroidal bubbles were also tested. These were like A in terms of internal properties and volume, but having a shape either flattened (oblate, O) or stretched (prolate, P) by a factor of two in the vertical.

The prolate bubble is concentrated into a smaller horizontal region than the spherical. Thus there may be a concentration of evaporative cooling effects as the bubble descends. This implies larger horizontal gradients during the descent/evolution, leading to increased mixing, and vice versa for the oblate bubble.

The initial prolate bubble has an vertical extent of 2 km and a width of approximately 700 m, so to some extent may resemble the flow from a smaller source of rain of several minutes duration.

The evolution of the various derived quantities is shown in Figure 12. The maximum cooling increases monotonically from O to P through the descent phase as the initial bubble lengthens and narrows. The descent velocity (to be shown in Section 5) intensifies in the same

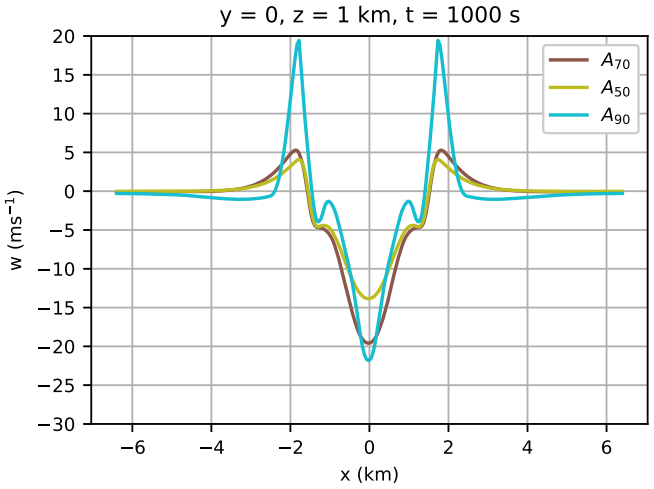

FIGURE 11 Vertical velocity profiles for A at various values of RH_e as indicated. These profiles are at a height of 1 km, horizontally through the centre of the domain, at the end of the experiment ($t = 1000$ s).

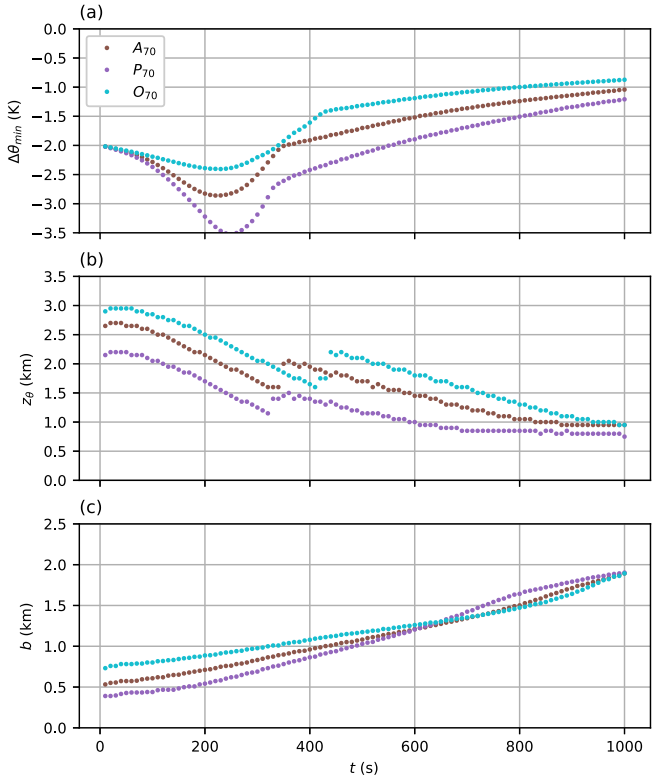

FIGURE 12 Time evolution of some quantities derived from A, O, and P at $RH_e = 70\%$. (a) Most negative θ perturbation in the domain, $\Delta\theta_{min}$. (b) Vertical position of the most negative θ perturbation, z_θ. (c) Downdraught radius b, defined as the maximum radius of any point with $\Delta\theta < 0.2\Delta\theta_{min}$.

trend. The geometric measures tend to converge on the whole, as the θ perturbation does at later times.

4.5 | Three-moment microphysics

As mentioned above, two-moment microphysics is commonly used in numerical weather modelling, and the results in previous subsections have been generated with MONC using two-moment CASIM. Three-moment microphysics is more computationally expensive, but reduces sedimentation rates compared with two-moment, which may be overly dispersive (Milbrandt & McTaggart-Cowan, 2010). To examine this aspect, the experiments were repeated with three-moment CASIM, and a comparison of the two modes is presented here and in the next section.

Figure 13 shows the three-moment equivalent of Figure 7, that is, experiments Z, A, and B at $RH_e = 70\%$ at time 300 s. The differences are most evident in the mass mixing ratio q_r, which has a more elongated vertical spread downwards in two-moment mode. This is greater for the run without evaporation (Z) and that with larger initial drop sizes (B). Despite the increased vertical dispersion of rain, the buoyancy fields are not very different, being dominated by the temperature/humidity perturbations. As the experiments evolve, the buoyancy fields remain quite close, so that the emerging cold-pool phase is very similar to that in two-moment mode shown in Figure 8.

To illustrate the differences further, the approximate drop diameter scale D^* (see Equation A12 in Appendix A) was calculated for experiments A_{70} and B_{70}, that is, bubbles with different initial drop-size distributions, for two- and three-moment CASIM. The results at 300 s are shown in Figure 14. It may be seen that the vertical dispersion is correlated with drop size and hence terminal velocity. Dispersion is greater in two-moment mode, particularly when the initial mean drop size is larger (with consequently greater fall speeds).

A broad comparison of the different CASIM modes will be presented in plots summarising all the experiments in the following section.

5 | SYNTHESIS OF RESULTS

In this section, results from more experiments with different values of RH_e are included, in addition to those already presented. These populate the parameter space further to help identify any trends in the data.

5.1 | Vertical velocity

A plot of the final centreline vertical velocities against RH_e for all experiments is shown in Figure 15. Figure 15a shows the two-moment results and Figure 15b the three-moment ones. In either mode there is a marked linear trend for configurations A and C, albeit with saturation at the extreme of high RH_e. In general, the three-moment results are similar to but slightly weaker than the two-moment results.

These experiments span two values of RH_b as well as the RH_e variation The differences in RH_b between A and C do not affect the correlation significantly, and probably bubble dilution by entrainment is the reason for this. The linearity is doubtless due in part to the idealised nature of these experiments, but indicates a trend that may be reflected in more realistic situations.

It is evident that the more humid environments produce more intense downdraughts. This agrees with the earlier finding that particle effects dominate the central core of the downdraught, while the θ perturbation contributes to the lateral growth of the thermal. Thus the reduced evaporation of drops in more moist environments

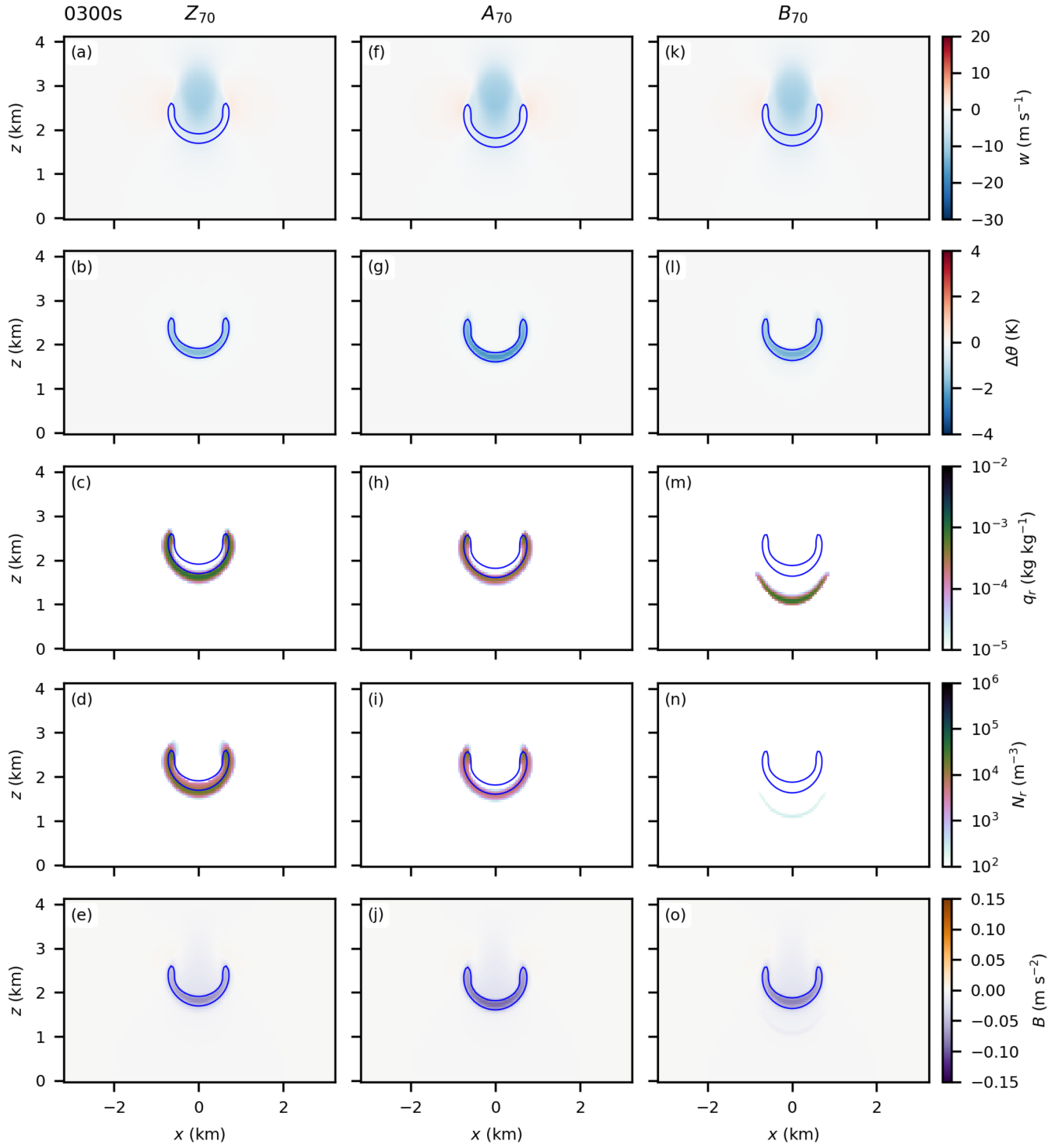

FIGURE 13 Simulation fields at 300 s for experiments Z, A, and B at $RH_e = 70\%$, using three-moment CASIM. Panels as in the two-moment equivalent, Figure 7.

may allow for an increase in gravity-driven momentum transfer from the drops to the atmosphere.

Downdraught intensity also increases as the bubble initial shape changes from oblate (O) through spherical (A) to prolate (P). The vertical passage of the same amount of rain and cold air through a smaller horizontal cross-section appears to reinforce the downdraught. This may indicate that longer-duration sources of rain will produce stronger downdraughts. The two-moment drop dispersion also tends to elongate the downdraught slightly, with the intensities being marginally greater than those for three-moment.

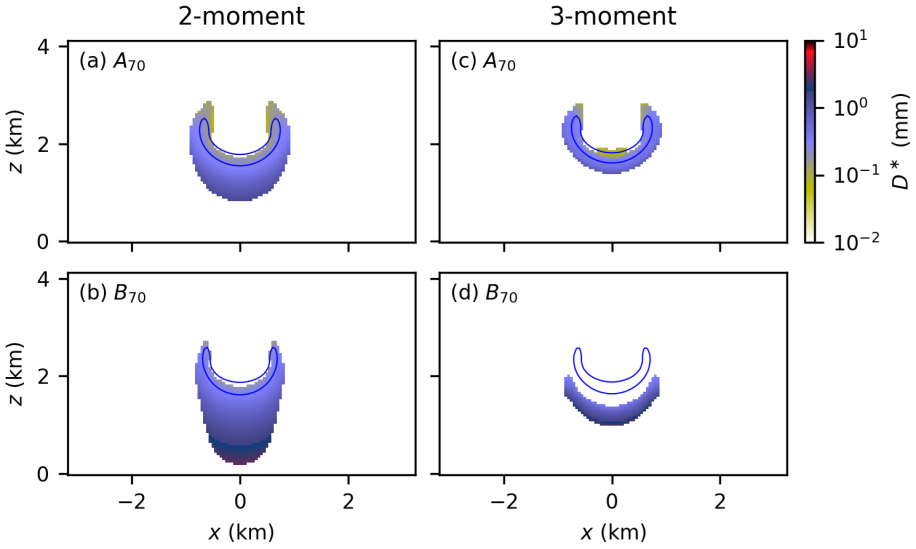

FIGURE 14 Approximate drop diameter scaling D^* (mm) at 300 s in the experiments A_{70} (top row) and B_{70} (bottom row). Panels (a,b) show two-moment CASIM and (c,d) show three-moment CASIM. As previously, contours indicate half the minimum $\Delta\theta$ in the domain at that time, for each experiment.

For the non-evaporating experiments X–Z, increased rain mass seems to be more of a controlling factor for downdraught velocity than the initial θ perturbation.

5.2 | Temperature

Figure 16 shows a plot of the final $\Delta\theta_{min}$ values against RH_e. Again, Figure 16a shows the two-moment results and Figure 16b the three-moment ones. This figure shows that, all other things being equal, drier environments lead to increased cooling. The trend in these experiments is not as pronounced as that for downdraught velocity, but in general that may depend on the details of the microphysics. As vertical velocity was reduced in the three-moment results, so cooling is increased, although the differences are generally small.

As would be expected, final $\Delta\theta_{min}$ depends on the initial bubble θ perturbation and the experiment details, with entrainment of the environment reducing the absolute temperature difference and evaporation tending to increase it. The values for A and B also show that drop size has an effect. This is presumably because smaller drops have a lower terminal velocity and hence increased residence time in the atmosphere, and also an increased surface area compared with the same mass of large drops, possibly allowing for more evaporation. This is consistent with previous findings: for example, Snook and Xue (2008). Reduced sedimentation rates in three-moment CASIM would also increase drop residence time, allowing for more evaporation. This may contribute to the opposite sense of the two- versus three-moment differences in w and $\Delta\theta$.

By contrast, the varying bubble shape seems to increase or decrease both effects simultaneously, with prolate bubbles having increased cooling as well as velocity, and vice versa for oblate. Development of increased horizontal gradients in the prolate bubbles may possibly promote more mixing and hence evaporative cooling, but apparently the width reduction and/or elongation avoids an associated penalty of reducing the downdraught velocity.

6 | CONCLUSIONS AND RECOMMENDATIONS FOR FUTURE WORK

In general, these idealised experiments show that an evaporating particulate phase increases the complexity of downdraught flow. The particulates intensify the downward momentum of the downdraught through acceleration of the flow due to their mass loading, up to the point where they may effectively suppress any downdraught vortex ring if the temperature perturbation is relatively weak. The depletion of the particulates by evaporation in drier environments is thus associated with a weakening of the downward momentum in the downdraught, at the same time as the overall cooling is increased.

A striking result is the effect of initial bubble shape. A narrower bubble of the same volume produces greater cooling and downward velocity. Horizontal scales of vertical motion in high-resolution numerical weather modelling have shown a tendency to correlate with the horizontal resolution of the model grid (Stein *et al.*, 2015). If the precipitation load of downdraughts is spread out more widely as a result of such aliasing, the downdraught evolution may be too weak as a consequence.

It is shown that a change in environmental conditions may intensify some aspects of the downdraught/cold-pool system while simultaneously weakening others, but this is also dependent on bubble shape. This finding may help

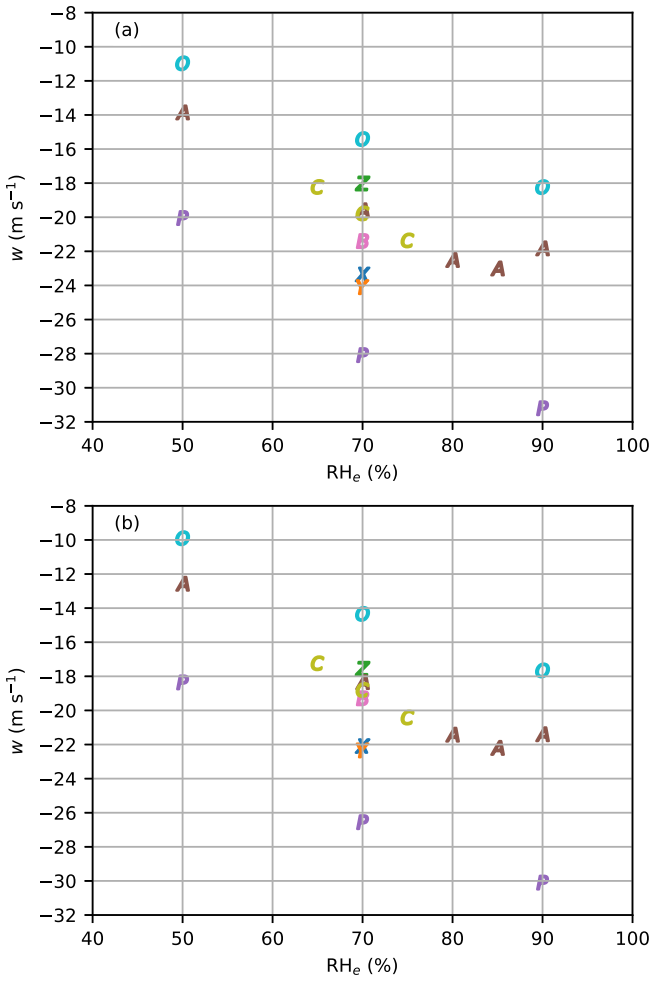

FIGURE 15 Scatter plot of final centreline velocity at 1 km altitude against RH_e for all experiments, indicated by letter. (a) Two-moment microphysics, (b) three-moment microphysics.

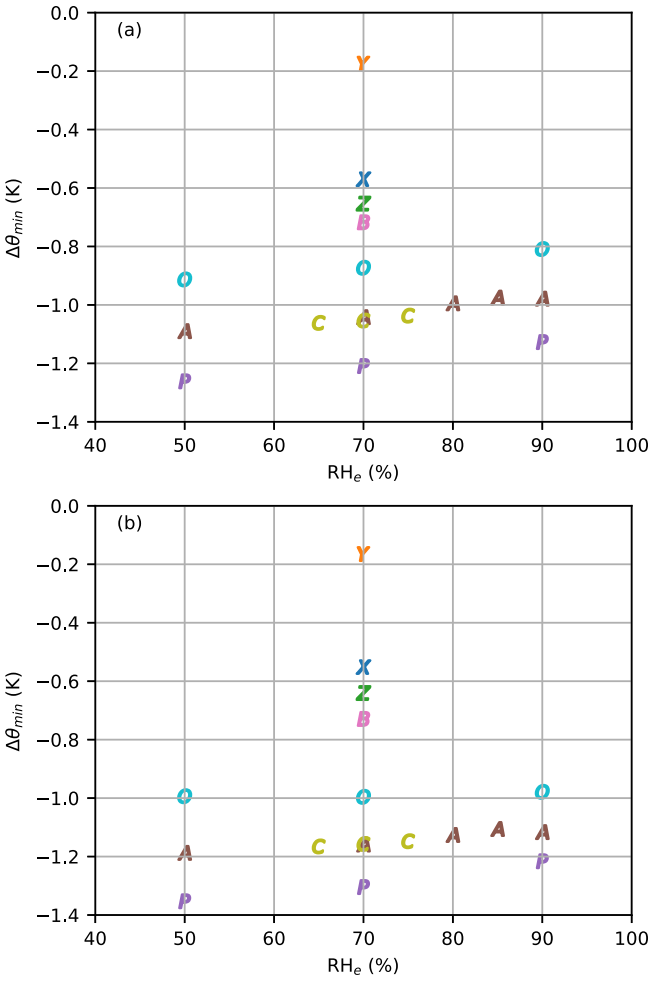

FIGURE 16 Scatter plot of final domain $\Delta\theta_{min}$ against RH_e for all experiments, indicated by letter. (a) Two-moment microphysics, (b) three-moment microphysics.

with the interpretation of previous studies, which have shown a divergence of sensitivities of downdraught intensity to the ambient conditions. It also emphasises the need to identify which system measures—such as downward momentum versus negative buoyancy—are most significant in any situation.

The cold-pool front may inherit differing "head" circulations and temperature perturbations from the impinging downdraught, depending on the conditions. The resulting vorticity/buoyancy balance of the front may have implications for its propagation (characterised by the Froude number), as discussed recently by Rooney (2023).

The spectrum of real, precipitating downdraughts probably contains elements similar to evaporating particle-laden thermals or plumes and particle swarms. Observed downdraught virga may be similar to the swarm of large drops ahead of the downdraught, and this may be the cause of their lacking a turbulent appearance. It is also possible that a more continuous stream of particles could induce a turbulent flow in the surrounding clear air (invisible to the observer of virga), after the manner of the bubble plume of McDougall (1978). The velocity of the air in the swarm is not necessarily large, but its wake, cooled by evaporation, may accelerate any following descending air. The laminar appearance of virga may be due to a combination of these factors.

In the presentation and interpretation of these results, it must be acknowledged that they are dependent on the parametrisations of the models, as demonstrated by the comparison of two- and three-moment CASIM modes. Nonetheless, this study could usefully be extended. Future work would explore the parameter space more fully, and bridge the gap between these simulations and more realistic downdraughts.

For a more complete exploration of parameter space, future work should define the initial regimes under which the thermal may be suppressed. As seen above, this has

implications for the radial spread of the downdraught and will also affect the structure of the resulting cold pool.

To bridge from these idealised simulations to more realistic conditions, there is a range of possibilities. Finite-duration sources of cooling and/or hydrometeors could be compared, for example, with vertically stretched bubbles. Simulations could be made less idealised through initial inhomogeneities in the bubble and/or environment: for example, particle-density variation or environmental temperature/density stratification.

Alternatively, downdraughts in high-resolution numerical weather simulations could be identified and analysed in the framework of this study, to see if similar features and/or regimes are observed. Deep downdraughts would also provide an opportunity to consider effects of ice microphysics further, which has not been investigated here (Engerer *et al.*, 2008; Gilmore *et al.*, 2004; Van Den Heever & Cotton, 2004). An extension of this would be to examine regime dependence on the conditions generating the downdraught. Overall, it would be useful to attempt to span the range of downdraught conditions, to assist with interpretation of apparently contradictory results in the literature.

AUTHOR CONTRIBUTIONS

G. G. Rooney: conceptualization; investigation; writing – original draft. **B. J. Shipway:** conceptualization; writing – review and editing. **D. J. Parker:** conceptualization; writing – review and editing.

ACKNOWLEDGEMENTS

Thanks to Adrian Hill, Paul Field, Steef Boeing, and Alison Stirling for helpful discussions. G. G. Rooney gratefully acknowledges the support of the Cheney Fellowship scheme at the University of Leeds. The reviewers are also gratefully acknowledged for their comments, which improved this study.

DATA AVAILABILITY STATEMENT

The data that support the findings of this study are available from the corresponding author upon reasonable request.

ORCID

G. G. Rooney https://orcid.org/0000-0002-3787-1198
D. J. Parker https://orcid.org/0000-0003-2335-8198

REFERENCES

Abel, S.J. & Shipway, B.J. (2007) A comparison of cloud-resolving model simulations of trade wind cumulus with aircraft observations taken during RICO. *Quarterly Journal of the Royal Meteorological Society*, 133(624), 781–794.

Andrejczuk, M., Grabowski, W.W., Malinowski, S.P. & Smolarkiewicz, P.K. (2004) Numerical simulation of cloud–clear air interfacial mixing. *Journal of the Atmospheric Sciences*, 61(14), 1726–1739.

Bloomfield, L.J. & Kerr, R.C. (2000) A theoretical model of a turbulent fountain. *Journal of Fluid Mechanics*, 424, 197–216.

Bolgiani, P., Fernández-González, S., Valero, F., Merino, A., García-Ortega, E., Sánchez, J.L. et al. (2020) Simulation of atmospheric microbursts using a numerical mesoscale model at high spatiotemporal resolution. *Journal of Geophysical Research: Atmospheres*, 125(4), e2019JD031791.

Bordoloi, A.D., Lai, C.C.K., Clark, L., Carrillo, G.V. & Variano, E. (2020) Turbulence statistics in a negatively buoyant multiphase plume. *Journal of Fluid Mechanics*, 896, A19.

Boufadel, M.C., Socolofsky, S., Katz, J., Yang, D., Daskiran, C. & Dewar, W. (2020) A review on multiphase underwater jets and plumes: Droplets, hydrodynamics, and chemistry. *Reviews of Geophysics*, 58, e2020RG000703.

Brown, N., Weiland, M., Hill, A., Shipway, B., Maynard, C., Allen, T. et al. (2020) A highly scalable Met Office NERC Cloud model. https://arxiv.org/abs/2009.12849

Brown, R.J., Bonadonna, C. & Durant, A.J. (2012) A review of volcanic ash aggregation. *Physics and Chemistry of the Earth, Parts A/B/C*, 45–46, 65–78.

Bush, J.W.M., Thurber, B.A. & Blanchette, F. (2003) Particle clouds in homogeneous and stratified environments. *Journal of Fluid Mechanics*, 489, 29–54.

Chandra, A.S., Zuidema, P., Krueger, S., Kochanski, A., de Szoeke, S.P. & Zhang, J. (2018) Moisture distributions in tropical cold pools from equatorial Indian Ocean observations and cloud-resolving simulations. *Journal of Geophysical Research: Atmospheres*, 123(20), 11,445–11,465.

Dawson, D.T., Mansell, E.R., Jung, Y., Wicker, L.J., Kumjian, M.R. & Xue, M. (2014) Low-level Z_DR signatures in supercell forward flanks: The role of size sorting and melting of hail. *Journal of the Atmospheric Sciences*, 71(1), 276–299.

Devenish, B.J., Bartello, P., Brenguier, J.-L., Collins, L.R., Grabowski, W.W., IJzermans, R.H.A. et al. (2012) Droplet growth in warm turbulent clouds. *Quarterly Journal of the Royal Meteorological Society*, 138(667), 1401–1429.

Devenish, B.J. & Cerminara, M. (2018) The transition from eruption column to umbrella cloud. *Journal of Geophysical Research: Solid Earth*, 123(12), 10,418–10,430.

Emanuel, K.A. (1994) *Atmospheric convection*. USA: Oxford University Press.

Engerer, N.A., Stensrud, D.J. & Coniglio, M.C. (2008) Surface characteristics of observed cold pools. *Monthly Weather Review*, 136(12), 4839–4849.

Field, P.R., Hill, A., Shipway, B., Furtado, K., Wilkinson, J., Miltenberger, A. et al. (2023) Implementation of a double moment cloud microphysics scheme in the UK met office regional numerical weather prediction model. *Quarterly Journal of the Royal Meteorological Society*, 149(752), 703–739.

Giangrande, S.E., Collis, S., Straka, J., Protat, A., Williams, C. & Krueger, S. (2013) A summary of convective-core vertical velocity properties using ARM UHF wind profilers in Oklahoma. *Journal of Applied Meteorology and Climatology*, 52(10), 2278–2295.

Gilmore, M.S., Straka, J.M. & Rasmussen, E.N. (2004) Precipitation and evolution sensitivity in simulated deep convective storms: Comparisons between liquid-only and simple ice and

liquid phase microphysics. *Monthly Weather Review*, 132(8), 1897–1916.

Grant, L.D. & van den Heever, S.C. (2018) Cold pool-land surface interactions in a dry continental environment. *Journal of Advances in Modeling Earth Systems*, 10(7), 1513–1526.

Hirt, M., Craig, G.C., Schäfer, S.A.K., Savre, J. & Heinze, R. (2020) Cold-pool-driven convective initiation: using causal graph analysis to determine what convection-permitting models are missing. *Quarterly Journal of the Royal Meteorological Society*, 146(730), 2205–2227.

James, R.P. & Markowski, P.M. (2010) A numerical investigation of the effects of dry air aloft on deep convection. *Monthly Weather Review*, 138(1), 140–161.

Joseph, J., Girishkumar, M.S., McPhaden, M.J. & Rao, E.P.R. (2021) Diurnal variability of atmospheric cold pool events and associated air-sea interactions in the Bay of Bengal during the summer monsoon. *Climate Dynamics*, 56, 837–853.

Kamburova, P.L. & Ludlam, F.H. (1966) Rainfall evaporation in thunderstorm downdraughts. *Quarterly Journal of the Royal Meteorological Society*, 92(394), 510–518.

Kirsch, B., Ament, F. & Hohenegger, C. (2021) Convective cold pools in long-term boundary layer mast observations. *Monthly Weather Review*, 149(3), 811–820.

Knupp, K.R. (1988) Downdrafts within high plains cumulonimbi. Part II: Dynamics and thermodynamics. *Journal of the Atmospheric Sciences*, 45, 3965–3982.

Knupp, K.R. & Cotton, W.R. (1985) Convective cloud downdraft structure: An interpretive survey. *Reviews of Geophysics*, 23(2), 183–215.

Kruse, I.L., Haerter, J.O. & Meyer, B. (2022) Cold pools over the Netherlands: A statistical study from tower and radar observations. *Quarterly Journal of the Royal Meteorological Society*, 148(743), 711–726.

Lai, A.C.H., Wang, R.-Q., Law, A.W.-K. & Adams, E.E. (2016) Modeling and experiments of polydisperse particle clouds. *Environmental Fluid Mechanics*, 16, 875–898.

Linden, P.F. & Simpson, J.E. (1985) Microbursts: a hazard for aircraft. *Nature*, 317, 601–602.

Liu, W., Dong, S., Zheng, J., Liu, C., Wang, C., Shangguan, W. et al. (2022) Quantifying the rainfall cooling effect: The importance of relative humidity in Guangdong, South China. *Journal of Hydrometeorology*, 23(6), 875–889.

Mallinson, H.M. & Lasher-Trapp, S.G. (2019) An investigation of hydrometeor latent cooling upon convective cold pool formation, sustainment, and properties. *Journal of the Atmospheric Sciences*, 147, 3205–3222.

McDougall, T.J. (1978) Bubble plumes in stratified environments. *Journal of Fluid Mechanics*, 85(4), 655–672.

McDougall, T.J. (1981) Negatively buoyant vertical jets. *Tellus*, 33(3), 313–320.

Milbrandt, J. & McTaggart-Cowan, R. (2010) Sedimentation-induced errors in bulk microphysics schemes. *Journal of the Atmospheric Sciences*, 67(12), 3931–3948.

Morrison, H. (2012) On the robustness of aerosol effects on an idealized supercell storm simulated with a cloud system-resolving model. *Atmospheric Chemistry and Physics*, 12(16), 7689–7705.

Proctor, F.H. (1989) Numerical simulations of an isolated microburst. part II: Sensitivity experiments. *Journal of the Atmospheric Sciences*, 46(14), 2143–2165.

Rio, C., Grandpeix, J.-Y., Hourdin, F., Guichard, F., Couvreux, F., Lafore, J.-P. et al. (2013) Control of deep convection by sub-cloud lifting processes: the ALP closure in the LMDZ5B general circulation model. *Climate Dynamics*, 40(9-10), 2271–2292.

Rogers, R.R. & Yau, M.K. (1989) *A short course in cloud physics*. Oxford: Butterworth-Heinemann.

Rooney, G.G. (2015) Descent and spread of negatively buoyant thermals. *Journal of Fluid Mechanics*, 780, 457–479.

Rooney, G.G. (2017) Haboobs, dust spouts and Lawrence of Arabia. *Weather*, 72(4), 107–110.

Rooney, G.G. (2023) Negatively buoyant vortices in the Boussinesq-Euler equations. *Physical Review Fluids*, 8(12), 123802.

Rooney, G.G., Stirling, A.J., Stratton, R.A. & Whitall, M. (2022) C-POOL: A scheme for modelling convective cold pools in the Met Office Unified Model. *Quarterly Journal of the Royal Meteorological Society*, 148(743), 962–980.

Ross, T.I.D. & Lasher-Trapp, S. (2024) On CCN effects upon convective cold pool timing and features. *Monthly Weather Review*, 152, 891–906.

Sakaeda, N. & Torri, G. (2023) The observed effects of cold pools on convection triggering and organization during DYNAMO/AMIE. *Journal of Geophysical Research: Atmospheres*, 128(17), e2023JD038635.

Schiro, K.A. & Neelin, J.D. (2018) Tropical continental downdraft characteristics: mesoscale systems versus unorganized convection. *Atmospheric Chemistry and Physics*, 18(3), 1997–2010.

Shipway, B.J. & Hill, A.A. (2012) Diagnosis of systematic differences between multiple parametrizations of warm rain microphysics using a kinematic framework. *Quarterly Journal of the Royal Meteorological Society*, 138(669), 2196–2211.

Slack, G.W. (1963) Sedimentation of a large number of particles as a cluster in air. *Nature*, 200(4913), 1306.

Snook, N. & Xue, M. (2008) Effects of microphysical drop size distribution on tornadogenesis in supercell thunderstorms. *Geophysical Research Letters*, 35(24), L24803.

Socolofsky, S.A. & Adams, E.E. (2005) Role of slip velocity in the behavior of stratified multiphase plumes. *Journal of Hydraulic Engineering*, 131(4), 273–282.

Srivastava, R.C. (1985) A simple model of evaporatively driven downdraft: Application to microburst downdraft. *Journal of Atmospheric Sciences*, 42(10), 1004–1023.

Srivastava, R.C. (1987) A model of intense downdrafts driven by the melting and evaporation of precipitation. *Journal of Atmospheric Sciences*, 44(13), 1752–1774.

Stein, T.H., Hogan, R.J., Clark, P.A., Halliwell, C.E., Hanley, K.E., Lean, H.W. et al. (2015) The DYMECS project: A statistical approach for the evaluation of convective storms in high-resolution NWP models. *Bulletin of the American Meteorological Society*, 96(6), 939–951.

Swann, H. (1998) Sensitivity to the representation of precipitating ice in CRM simulations of deep convection. *Atmospheric Research*, 47–48, 415–435.

Takeda, T. (1966) The downdraft in the convective cloud and raindrops: A numerical computation. *Journal of the Meteorological Society of Japan. Ser. II*, 44(1), 1–11.

Takemi, T. (2006) Impacts of moisture profile on the evolution and organization of midlatitude squall lines under various shear conditions. *Atmospheric Research*, 82(1–2), 37–54.

Torri, G. & Kuang, Z. (2016) A Lagrangian study of precipitation-driven downdrafts. *Journal of Atmospheric Sciences*, 73, 839–854.
Torri, G. & Kuang, Z. (2017) Corrigendum. *Journal of Atmospheric Sciences*, 74, 3125–3126.
Tsonis, A.A. (2007) *An introduction to atmospheric thermodynamics*. Cambridge: Cambridge University Press.
Vaillancourt, P.A. & Yau, M.K. (2000) Review of particle-turbulence interactions and consequences for cloud physics. *Bulletin of the American Meteorological Society*, 81(2), 285–298.
Van Den Heever, S.C. & Cotton, W.R. (2004) The impact of hail size on simulated supercell storms. *Journal of the Atmospheric Sciences*, 61(13), 1596–1609.
Wakimoto, R.M. (2001) Convectively driven high wind events. *Meteorological Monographs*, 28(50), 255–298.
Wilson, J.W. & Wakimoto, R.M. (2001) The discovery of the downburst: T.T. Fujita's contribution. *Bulletin of the American Meteorological Society*, 82(1), 49–62.
Windmiller, J.M., Bao, J., Sherwood, S.C., Schanzer, T.D. & Fuchs, D. (2023) Predicting convective downdrafts from updrafts and environmental conditions in a global storm resolving simulation. *Journal of Advances in Modeling Earth Systems*, 15(3), e2022MS003048.
Woods, A.W. & Bursik, M.I. (1991) Particle fallout, thermal disequilibrium and volcanic plumes. *Bulletin of Volcanology*, 53, 559–570.
Yang, D., Chen, B., Socolofsky, S.A., Chamecki, M. & Meneveau, C. (2016) Large-eddy simulation and parameterization of buoyant plume dynamics in stratified flow. *Journal of Fluid Mechanics*, 794, 798–833.

How to cite this article: Rooney, G.G., Shipway, B.J. & Parker, D.J. (2025) Rain in convective downdraughts. *Quarterly Journal of the Royal Meteorological Society*, 1–20. Available from: https://doi.org/10.1002/qj.4923

APPENDIX A. INITIAL DROP CONDITIONS

CASIM uses the gamma distribution to describe the number of drops N as a function of drop diameter D, per cubic metre:

$$N(D) = N_r \frac{\lambda^{1+\mu}}{\Gamma(1+\mu)} D^{\mu} e^{-\lambda D}. \tag{A1}$$

Shipway and Hill (2012) define μ as the *shape parameter* and λ as the *slope parameter*. N_r is the number of raindrops per cubic metre, or number density.

Since

$$\begin{aligned} D^p N(D) &= N_r \frac{\lambda^{1+\mu}}{\Gamma(1+\mu)} D^{\mu+p} e^{-\lambda D} \\ &= \frac{\Gamma(1+\mu+p)}{\lambda^p\,\Gamma(1+\mu)}\, N_r \frac{\lambda^{1+\mu+p}}{\Gamma(1+\mu+p)}\, D^{\mu+p} e^{-\lambda D}, \end{aligned} \tag{A2}$$

then the pth moment of the distribution is given by

$$M(p) \equiv \int_0^{\infty} D^p N(D)\, dD = \frac{N_r}{\lambda^p} \frac{\Gamma(1+\mu+p)}{\Gamma(1+\mu)}. \tag{A3}$$

By definition, $\Gamma(z+1) = z\,\Gamma(z)$, and so $M(p)$ may be simplified for integer values of p,

$$M(p) = \frac{N_r}{\lambda^p} \prod_{i=1}^{p} (\mu + i) \qquad \text{for } p \in \mathbb{N}. \tag{A4}$$

The mode diameter of the gamma distribution is

$$D_Z = \frac{\mu}{\lambda}. \tag{A5}$$

The mean diameter is obtained from the first moment,

$$\overline{D} = \frac{M(1)}{N_r} = \frac{\mu+1}{\lambda}. \tag{A6}$$

As Shipway and Hill (2012) state, given a mass–diameter relationship of the form

$$m(D) = c\, D^d, \tag{A7}$$

then the bulk mass mixing ratio of the rain distribution is related to the dth moment by

$$q_r = \frac{cM(d)}{\rho_a}, \tag{A8}$$

where ρ_a is the air density. Making the assumption that (small) raindrops are spherical, then $d = 3$, that is, the mass mixing ratio is proportional to the third moment,

$$M(3) = \frac{N_r}{\lambda^3}(\mu+1)(\mu+2)(\mu+3), \tag{A9}$$

and $c = (\pi/6)\rho_w$, where ρ_w is the density of rainwater.

Given N_r, q_r, μ, c, and ρ_a, the value of λ may be readily obtained:

$$\lambda = \left(\frac{\pi}{6} \frac{\rho_w}{\rho_a} \frac{N_r}{q_r} (\mu+1)(\mu+2)(\mu+3) \right)^{1/3}. \tag{A10}$$

(It may be remarked that substituting $\nu = \mu + 2$ yields the "depressed" cubic equation

$$\nu^3 - \nu - \left(\frac{6}{\pi} \frac{\rho_a}{\rho_w} \frac{q_r}{N_r} \right) \lambda^3 = 0, \tag{A11}$$

which is potentially useful for finding μ if required.)

An approximate drop diameter scaling may be calculated from the mass and number of drops as

$$D^* = \left(\frac{\rho_a\, q_r}{\rho_w N_r} \right)^{1/3}. \tag{A12}$$

From above, it can be seen that this is equivalent to $D^* = \lambda^{-1}(\pi/6)^{1/3}(\nu^3 - \nu)^{1/3}$, compared with $\overline{D} = \lambda^{-1}(\nu - 1)$. These two measures are consequently quite similar.

For all the experiments, μ is initialised to the default value of 2.5 (Swann, 1998). From Table 1 and (A10), the initial values of λ are then approximately $1.4{\times}10^4$ and $3.6{\times}10^3\ \mathrm{m}^{-1}$ for small and large drops, respectively. The mode and mean diameters for the small drops are then 0.18 and 0.25 mm, and 0.7 and 1 mm for the large drops. The terminal velocities for these are expected to be within the range 0.1–10 $\mathrm{m}\cdot\mathrm{s}^{-1}$ (Abel & Shipway, 2007).

For three-moment rain, the initial value of the sixth moment (which is moment #3 in the three-moment scheme) may be obtained from (A4), noting that $\prod_{i=1}^{6}(\mu + i) \approx 3.59 \times 10^4$. The sixth power of λ in the denominator produces a very small initial numerical value.

APPENDIX B. SPHEROIDAL BUBBLES

For a spheroid with rotational symmetry about a vertical axis, the vertical semi-axis may be denoted r_v and the horizontal semi-axes will be equal and may be denoted r_h.

Compared with a sphere of radius r_s, the volumes will be equal if $r_\mathrm{s}^3 = r_\mathrm{h}^2 r_\mathrm{v}$.

Thus, for an equal-volume spheroid in which $r_\mathrm{h} = \phi r_\mathrm{s}$, then $r_\mathrm{v} = r_\mathrm{s}/\phi^2$. For example, halving the horizontal extent requires quadrupling the vertical extent to keep the volume the same.